

## Article

# Super Bonding Strength of Al<sub>2</sub>O<sub>3</sub> Nanoparticles Reinforced Sn Interlayer Steel/Aluminum Bimetal Casting

Mohamed Ramadan <sup>1,2,\*</sup>, Abdul Khaliq <sup>1,3,\*</sup>, K. M. Hafez <sup>2</sup>, Abdulaziz S. Alghamdi <sup>1</sup>, Naglaa Fathy <sup>4</sup>, Farid A. Harraz <sup>2,5</sup>, Badreddine Ayadi <sup>1</sup> and K. S. Abdel Halim <sup>1,2</sup>

- <sup>1</sup> College of Engineering, University of Ha'il, P.O. Box 2440, Hail 81441, Saudi Arabia; a.alghamdi@uoh.edu.sa (A.S.A.); b.ayadi@uoh.edu.sa (B.A.); k.abdulhalem@uoh.edu.sa (K.S.A.H.)
- <sup>2</sup> Central Metallurgical Research and Development Institute (CMRDI), P.O. Box 87, Helwan 11421, Egypt; khalidhafez@yahoo.com (K.M.H.); fharraz68@yahoo.com (F.A.H.)
- <sup>3</sup> School of Engineering, RMIT University, Melbourne, VIC 3000, Australia
- <sup>4</sup> Department of Physics, College of Science, University of Hail, P.O. Box 2440, Hail 81441, Saudi Arabia; naglaaf2002@yahoo.com
- <sup>5</sup> Promising Centre for Sensors and Electronic Devices (PCSED), Advanced Materials and Nano-Research Centre, Najran University, P.O. Box 1988, Najran 11001, Saudi Arabia
- \* Correspondence: mnrnais3@yahoo.com (M.R.); ab.ismail@uoh.edu.sa (A.K.); Tel.: +966-556-873-356 (A.K.)

**Abstract:** For specialized applications, it is incumbent to develop new materials that enable manufacturers to develop new processes and designs. For better fuel economy, structural integrity, and lightweight applications, the development of bimetallic steel/aluminum (Al) alloys having a strong interfacial bond is required. Therefore, a mild steel/Al-bearing alloy bimetallic composite was investigated in this study. Firstly, a tin (Sn) interlayer was developed between the steel substrate and the Al-bearing alloy by the tinning process. For further improvement in the interfacial integrity, alumina (Al<sub>2</sub>O<sub>3</sub>) nanoparticles were added to the Sn powder during the tinning process. Four different wt.% of Al<sub>2</sub>O<sub>3</sub> nanoparticles of 0.25, 0.5, 1, and 1.5 were added and mixed thoroughly with Sn powder before mixing them with flux prior to the tinning process. Finally, molten Al-bearing alloy (Al–Sn–Si–Cu) was poured over the Al<sub>2</sub>O<sub>3</sub> nanoparticles reinforced tinned steel substrate. A cross-section of the steel/Al-bearing alloy bimetallic composite was prepared for optical microscopy (OM), scanning electron microscopy (SEM), energy-dispersive X-ray spectroscopy (EDS), and shear testing. The cross-section microstructure of the steel/Al-bearing alloy bimetallic composite revealed irregular and discontinuous interfacial layers in the case of the low-temperature (170 °C) tinning process. However, a uniform, continuous interfacial layer was fabricated during the tinning process when additional preheat to the steel substrate and tinning process was adopted. It can be reported that low Al<sub>2</sub>O<sub>3</sub> nanoparticles loading (0.25%) and steel substrate preheating were recommended for the better interfacial layer in the steel/Al-bearing alloy bimetallic composite.

**Keywords:** super bonding; aluminum; steel; bimetallic; Al<sub>2</sub>O<sub>3</sub>; nanoparticles; Sn; interlayer



**Citation:** Ramadan, M.; Khaliq, A.; Hafez, K.M.; Alghamdi, A.S.; Fathy, N.; Harraz, F.A.; Ayadi, B.; Abdel Halim, K.S. Super Bonding Strength of Al<sub>2</sub>O<sub>3</sub> Nanoparticles Reinforced Sn Interlayer Steel/Aluminum Bimetal Casting. *Crystals* **2022**, *12*, 324. <https://doi.org/10.3390/cryst12030324>

Academic Editor: Bolv Xiao

Received: 5 February 2022

Accepted: 24 February 2022

Published: 26 February 2022

**Publisher's Note:** MDPI stays neutral with regard to jurisdictional claims in published maps and institutional affiliations.



**Copyright:** © 2022 by the authors. Licensee MDPI, Basel, Switzerland. This article is an open access article distributed under the terms and conditions of the Creative Commons Attribution (CC BY) license (<https://creativecommons.org/licenses/by/4.0/>).

## 1. Introduction

Nowadays, manufacturing techniques are more focused on fabricating materials of superior properties along with the facilitation of their fabrication techniques. Although several researchers [1–3] performed intensive development of cast metals structures and properties, the possibilities of the existing monometallic alloys are practically exhausted for fabricating new materials offering superior properties.

Liquid–solid compound casting has been used to fabricate different ferrous and nonferrous functionally grade materials, which was found to be the most economical fabrication technique that allows the fabrication of bimetal directly [4–6]. The higher bonding strength of bimetallic materials is still required to meet the demand of specialized applications. More attention should be given to improving the interfacial bonding strength of the metallic

bearing material and the metallic substrate. Nanotechnology is a promising technology for the fabrication of products of determining functions. Nanomaterials are also used in cast metals (e.g., in cast metal structure with nanocrystalline precipitates) and in molding sand technologies, due to their special and superior effect of cast metal properties [7].

Ferrous alloys are still the most widely used metallic materials in casting processes [8–12]. The advantages of ferrous metals are that they are unique, low in cost, and stable in performance. Ferrous metals play significant roles in engineering manufacturing [13]. High-strength steel is an important engineering material for any national economy, national security, and a variety of key engineering areas.

The mechanisms of strengthening the metals are categorized as dislocation, grain refinement, solution strengthening, and second-phase dispersion, as well as phase transformation strengthening [14,15]. Although second-phase dispersion improves the strengths of the metals, the reduction in plasticity and/or toughness of the ferrous and nonferrous metals are often observed. It was reported [16,17] that the strength, along with toughness improvements of metals and alloys, could be achieved by grain refinement strengthening due to the influence of grain refining and pinning grain boundaries of the fine second phase particle to hinder coarsening of microstructure that can compensate toughness depreciation. Therefore, second-phase dispersion and grain refinement strengthening are considered the most important mechanisms for strengthening and toughening ferrous metallic materials [18].

Alloying, nucleating agents, as well as particles reinforcements, can be introduced and/or precipitated in the second phase in the matrix of steel. The strengthening effect of nanoreinforcement is relatively higher than micro-sized reinforcement. The high surface energy of nanosized reinforcements and variation in specific gravity for liquid ferrous metals and reinforcement make the dispersion and distribution of nanosized reinforcements in the ferrous metallic matrix relatively difficult to achieve [19]. The methods for introducing nanoparticles into ferrous materials (cast steel and cast iron) are classified into four categories: internal, external nanoparticle methods, in situ additive manufacturing, and reaction methods. Using nanoparticles as strengthening phase or nucleation phase, the lattice mismatch and valence electron between nanoparticles, and crystal structure matrix of steel are important criteria for strengthening effect and analyzing nucleation efficiency. During solidification of molten steel at higher temperatures, the different carbon content produces ferrite or austenite primary phase. Therefore,  $\delta$ -Fe and/or  $\gamma$ -Fe are expected for nucleation. The effectiveness of heterogeneous nucleation and lattice mismatches relationship should be considered during the selection of nanoparticles suitable for the nucleating phase.

In two-layered bimetallic bearings, two metal alloys having different mechanical and wear properties are bonded together for heavyweights and stress-loading conditions. Two-layered bimetallic bearings are more suitable for medium-speed, medium-load, low-speed, and high-load situations. Bimetal bearings have the main functions of reducing friction and carrying loads of the shaft or any other axial and radial loading of moving parts. Low-carbon steel and stainless steel are commonly used as the base materials (substrates) in bimetallic bearings that are covered with Sn-based alloys, Al–Sn alloys, and Cu–Sn alloys on the exterior surface. The interfacial microstructure and the bond strength of bimetallic bearing materials were predominantly affected by substrate surface preparation, interlayer materials, and process parameters. The bonding quality of the bimetallic bearing materials fabricated by liquid–solid compound casting is dependent on various factors such as volume of liquid–solid ratio, the surface morphology of the solid substrate, and surface treatments of solid substrate [20–23]. Surface treatment of solid substrate could be performed by depositing a thin layer of Zn, Sn, and Al, using galvanizing, tinning, and aluminizing processes consequently [21–24].

In this study,  $\text{Al}_2\text{O}_3$  nanoparticles reinforced Sn interlayer were investigated through changing the processing parameters with an ultimate objective to improve the bonding strength of aluminum/steel bimetallic casting.

## 2. Materials and Methods

### 2.1. Materials

Aluminum/steel bimetallic specimens were prepared using the compound casting technique. Table 1 shows the chemical compositions of the Al-bearing alloy and carbon steel substrate used for Al/Steel bimetallic composite fabrication.

**Table 1.** Chemical composition of the carbon steel substrate, wt.%.

Chemical Composition	C	Sn	Si	Mn	Cu	Cr	Ni	Al	Fe
Al-bearing alloy	-	12	4		1	-	-	Bal.	-
Steel substrate	0.14	-	0.30	0.41	0.20	0.14	0.09	-	Bal.

### 2.2. Casting Process

Carbon steel specimen substrates of  $90 \times 25 \times 5 \text{ mm}^3$  were ground with emery papers of up to 800 grades. Steel specimen substrates were coated by pure tin and with a tin containing different percentages of alumina nanoparticles (50 nm). The direct pre-tinning process of the carbon steel substrate that involves powder tin, alumina nanoparticles, and flux mixture has been explained in detail elsewhere [25–29]. To study the process parameters on interfacial structure and bonding strength of Al/steel bimetallic casting, two different groups of bimetallic casting were prepared. In the bimetal A group, during the tinning process, steel substrates were heated at 350 °C for 120 s. For the bimetal B group, steel substrates were heated at 350 °C for 180 s, as shown in Table 2. A charge of 1.2 kg of Al-12Sn-4Si-1Cu bearing alloy was melted in an electrical furnace to 750 °C and 800 °C (heating rate = 10 °C/min.) in a graphite crucible for the bimetallic casting of group A and group B, respectively. After 30 min holding time, the molten Al alloy was poured on tinned carbon steel substrates, which were inserted into a preheated metallic mold at 170 °C and 350 °C. Figure 1 shows metallic mold steel substrate after cutting, steel substrate after grinding, steel substrate after tinning, the insertion of tinned steel substrate into the mold cavity, fabrication of bimetallic casting, and finally, the pouring process of molten Al-bearing alloy onto the metallic mold. Volume ratios of liquid Al-bearing alloy/solid carbon steel substrate were kept constant ( $V_L/V_S = 7$ ) for all fabricated bimetallic castings. The tinned steel solid substrate strips for both bimetals A and B were preheated using a hot plate for 120 s and 180 s at 350 °C before pouring liquid Al alloy. Six different pre-tinning and process parameters conditions of steel solid substrates and Al-bearing alloy were performed, as shown in Table 3.

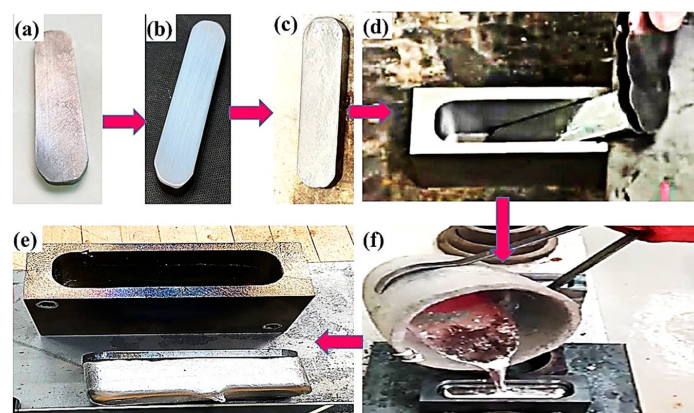


**Figure 1.** Aluminum/steel bimetal casting: (a) steel substrate after cutting; (b) steel substrate after grinding; (c) steel substrate after tinning; (d) tinned steel substrate was inserted into the metallic mold; (e) fabricated bimetallic casting; (f) molten Al alloy was poured into the metallic mold.

**Table 2.** Process parameters for two different bimetal castings groups.

Casting Process Designation	Tinning Process		Tinned Steel Preheating		Pouring Temp. °C	Mould Preheating Temp. °C
	Temp, °C	Time, s	Temp, °C	Time, s	Temp, °C	Temp, °C
Bimetal A	350	120	350	120	720	170
Bimetal B	350	180	350	180	770	350

**Table 3.** Pre-tinning interlayer and processing conditions of the steel solid substrate and Al-bearing alloy for six specimens.

S.N.	Pre-Tinning and Process Parameters Conditions
Specimen 0 (S0)	Bimetal with Process parameters A using pure Sn interlayer, bimetal A
Specimen 1 (S1)	Bimetal with Process parameters B using pure Sn interlayer, bimetal B
Specimen 2 (S2)	Bimetal with Process parameters B using Sn + 0.25 alumina nanoparticles interlayer
Specimen 3 (S3)	Bimetal with Process parameters B using Sn + 0.50 alumina nanoparticles interlayer
Specimen 4 (S4)	Bimetal with Process parameters B using Sn + 1.00 alumina nanoparticles interlayer
Specimen 5 (S5)	Bimetal with Process parameters B using Sn + 1.50 alumina nanoparticles interlayer

### 2.3. Microstructural Evaluations

For microstructural investigation, the specimens were cut, ground, polished, and etched with a solution consisting of 0.5 mL HNO<sub>3</sub>, 0.3 mL HCl, 0.2 mL HF and 19 mL H<sub>2</sub>O. An optical microscope (OM) (Olympus GX51, Tokyo, Japan) and field-emission scanning electron microscope (FESEM) (JEOL-6300F, 5 KV) coupled with energy-dispersive X-ray spectroscopy (EDS) scanning electron microscope (SEM) was used to investigate bimetallic materials and their interfacial structure. The chemical compositions of the bimetallic interfaces were measured by energy-dispersive X-ray spectroscopy (EDS).

### 2.4. Mechanical Characterizations

The shear strength value of the interface of the bimetallic specimen was performed using a universal tensile testing machine (Instron 5969, Instron with a maximum load of 50 KN, Norwood, MA, USA), as discussed in a previous study, along with the dimensions of the tensile–shear specimen [30]. All shear tests were performed at a constant strain rate of 0.5 mm/min to the failure of the specimens. Three specimens were tested to determine the average shear strength value.

## 3. Results

### 3.1. Microstructure and Mechanical Properties of Starting Materials

Tension strengths and hardness's of Al–Sn bearing alloy ( $110 \pm 5$  MPa and  $36.40 \pm 5.6$  HRF) and carbon steel substrate ( $410 \pm 10$  MPa,  $102.48 \pm 9.5$  HRF) used for bimetallic fabrication were measured according to (ASTM E8). Typical microstructures of the Al-bearing alloy and low carbon steel are shown in Figure 2. The alloying elements Si and Sn have limited solubility in Al at room temperature. Such elements precipitate as separate phases (Sn and Si) during the solidification process. Hence,  $\delta$ -Sn and  $\delta$ -Si segregate at the dendritic regions of  $\alpha$ -Al, as shown in Figure 2a. Binary intermetal of Cu–Sn (Cu<sub>6</sub>Sn<sub>5</sub>) is also present as high aspect ratio particles. The mild carbon steel optical microstructure is shown in Figure 2b, which reveals typical ferrite and pearlite phases. Figure 2b shows a typical microstructure of the mild steel substrate used in this study. The relative proportion of ferrite (white phase) and pearlite (black phase) confirms C contents in the steel.

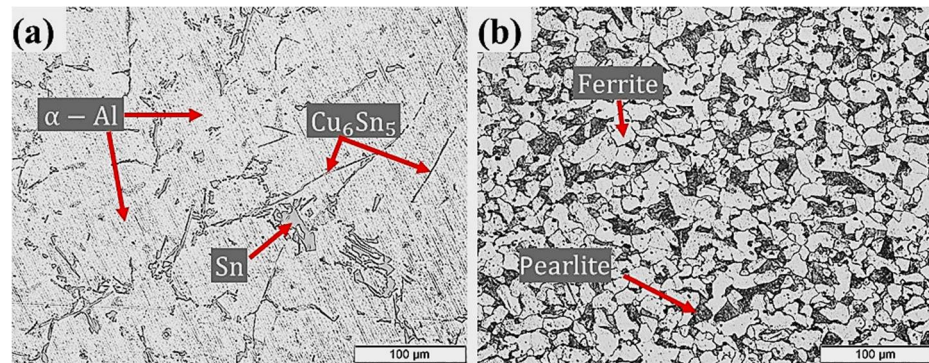


**Figure 2.** Microstructures of (a) Al-bearing alloy and (b) steel substrate, used for preparing bimetallic casting.

SEM and EDS analyses of the Al-bearing alloy are given in Figure 3. The black regions represent  $\alpha$ -Al, whereas the white spots depict Sn, and Si precipitates. Figure 3b reveals the qualitative chemical composition of the Al matrix that is predominantly composed of Al in addition to Si, Sn, and Cu. The white regions EDS analysis reveals that Sn is the main precipitated phase in the  $\alpha$ -Al interdendritic regions. Si phase also precipitates in a similar fashion. The needle-like phases are most likely  $\text{Cu}_2\text{Al}$  and  $\text{Cu}_6\text{Sn}_5$ , which are shown in Figure 3a.

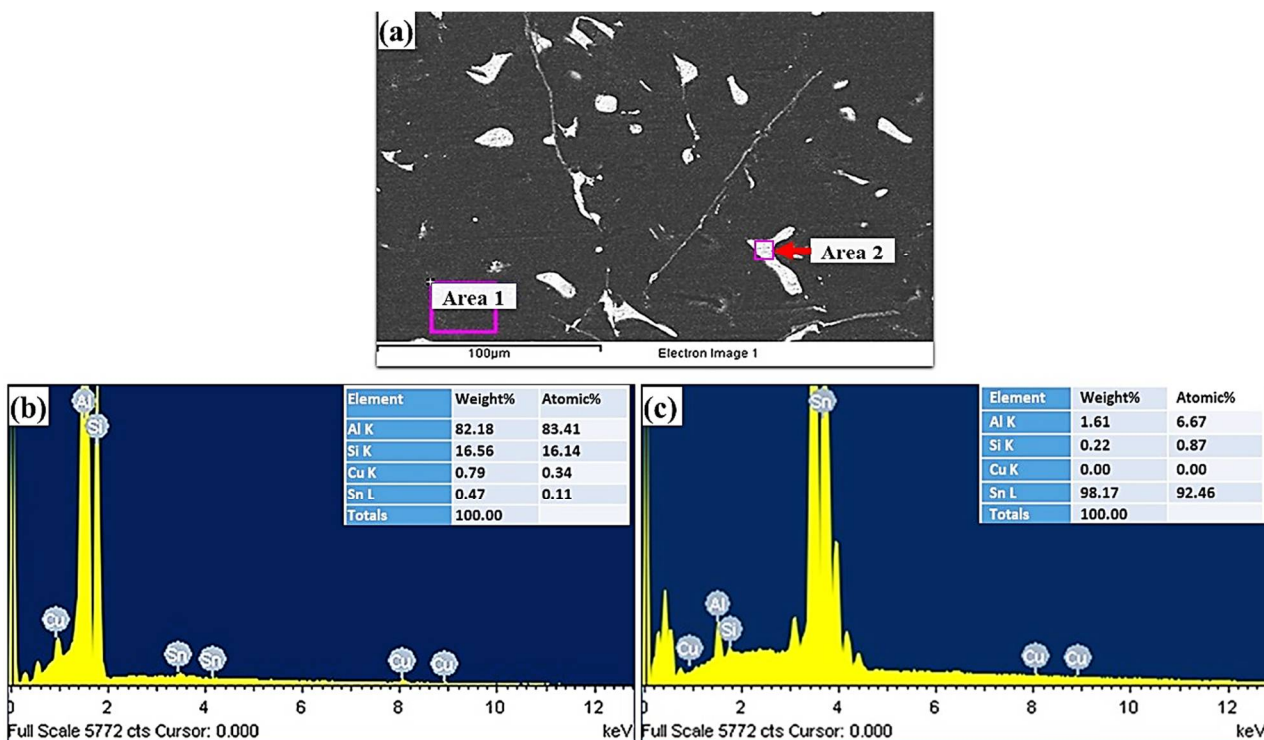


**Figure 3.** (a) SEM images of Al-bearing alloy and (b,c) graphical presentation of EDS microanalysis of the matrix (area 1) and precipitates (area 2).

### 3.2. Effect of Casting Process Parameters

In the present study, two casting parameters were investigated that are outlined in Table 2. For both bimetal A and B, a pure tin layer was developed on the steel substrate using the tinning process. For bimetal A (designated as S0), tinning was carried out at 350 °C for 120 s. The tinned steel substrate was preheated to 350 °C for 120 s before placing it in the preheated mold (170 °C). The final step involved the pouring of molten

Al-bearing alloy at 720 °C on the tinned steel substrate. The whole assembly was then allowed to cool naturally. A cross-section of the bimetal A was prepared for metallography study. Figure 4a shows the OM image of the bimetal A (S0) cross-section composed of the steel substrate, interfacial alloy layer, and Al-bearing alloy. The interfacial alloy layer morphology revealed that the adhesion between the steel substrate and Al-bearing alloy is uneven and discontinuous. This suggests marginal wetting between substrate and coating alloy that resulted in a poor interfacial bond. In Figure 4a, unbonded interfacial regions are evident. Overall, the thickness of the interfacial alloy layer is <math><4\text{--}5\ \mu\text{m}</math>. The interfacial alloy layer is most likely composed of Al–Fe ( $\text{Al}_3\text{Fe}$  and  $\text{Al}_5\text{Fe}_2$ ) intermetallic compounds, as reported by previous researchers [31].

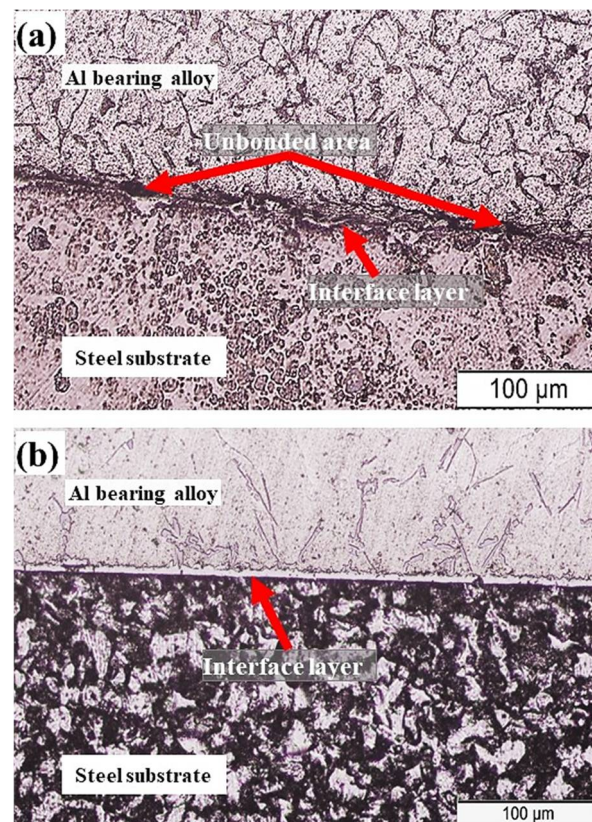
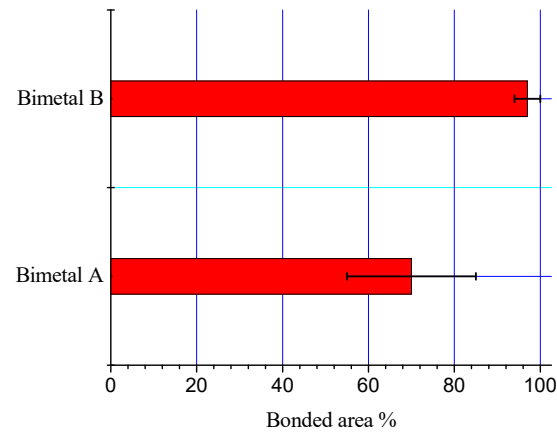


Figure 4. OM image of bimetal composites: (a) bimetal A and (b) bimetal B.

Figure 4b shows the OM image of bimetal B (S1). A similar tinning process produced this bimetal; however, 180 s was the holding time. Moreover, 350 °C for 180 s was the preheating temperature. In addition to that, mold was preheated to 350 °C prior to pouring of the molten Al-bearing alloy at 770 °C. The solidification and samples preparation procedures were unchanged. Typical microstructures of mild carbon steel substrate and Al-bearing alloy, in addition to interfacial alloy layer, were observed, as shown in Figure 4b. Contrary to bimetal A, the interfacial alloy layer formed in bimetal B is uniform and continuous. It has been reported earlier that the  $\text{FeSn}_2$  layer formed during the tinning process [28]. The additional supplied heat facilitated molten Al mass transfer to the steel substrate through the molten Sn/FeSn<sub>2</sub> layer. As a result, Al and Fe reacted, developing an alloy layer composed of  $\text{Al}_3\text{Fe}/\text{Al}_5\text{Fe}_2$  between the steel substrate and Al-bearing alloy. One study reported in the literature [32] suggested that the chemical reaction between Al and Fe is extremely fast and, therefore, is not the rate-limiting factor. However, in most cases, mass transfer of Al and Fe are the rate-limiting factors, as observed in this study.

The processing parameters significantly affected the morphology and thickness of the interfacial alloy layer. The bonded areas for both processing conditions (bimetal A and bimetal B) were calculated and are shown in Figure 5. The percentage of bonded area for

bimetal B is much higher than that in bimetal A. An increase of 33% bonded area in the case of bimetal B supports the argument that diffusion of the molten Al atoms through the liquid Sn layer facilitated for homogenous and regular interfacial alloy layer.



**Figure 5.** Bonded area in the samples S0 and S1.

A shear stress test is used to investigate the integrity of the interfacial alloy layer developed in a bimetal composite material. Figure 6 shows the influence of the processing parameters (Table 2) on the shear stress endurance of the interfacial alloy layer formed in the Al-bearing alloy and mild steel composite. An extraordinary difference in the shear stress–strain behavior of both processing conditions was recorded, which is evident from Figure 6. For the processing condition “A” (bimetal A), the Al-bearing alloy/mild steel composite failed at only 8 MPa shear stress with only 0.02 shear strain. However, for the processing condition “B” (bimetal B), the same bimetal composite failed at >30 MPa shear stress, with 0.11 shear strain. This is an increase of >280% in shear stress and >500% in the shear strain, which is a remarkable finding of this study.

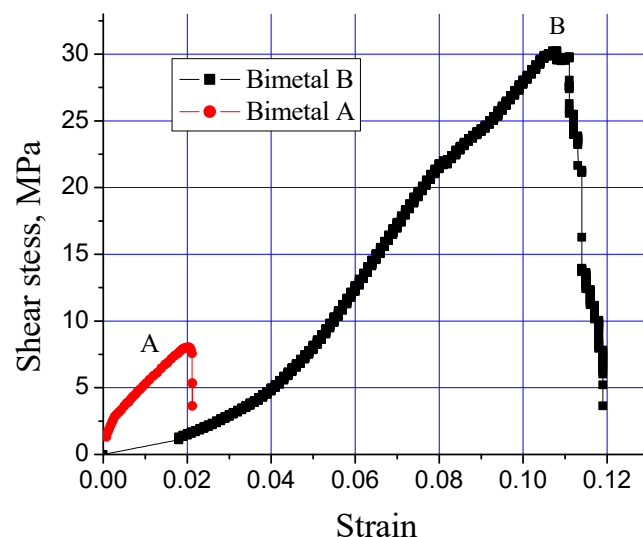


**Figure 6.** Effect of processing parameters on interfacial shear stress of Al-bearing alloy/carbon steel bimetallic composites, S0 and S1.

A comparative analysis of the processing conditions A and B suggested that the bimetal fabricated adopting route B produced a regular and uniform interfacial compound layer. This resulted in a larger bonded area between the Al-bearing alloy and mild steel bimetal composite. Hence, Al-bearing alloy/mild steel composite with significantly superior mechanical properties was successfully fabricated in this study. Therefore, bimetal B

was selected for further study, in which different loadings of  $\text{Al}_2\text{O}_3$  nanoparticles were performed to fabricate nanocomposites interlayer bimetallic materials.

### 3.3. Effect of Alumina Nanoparticle-Reinforced Sn Interlayer

#### 3.3.1. Microstructure and Interface Structure

This section outlines the influence of  $\text{Al}_2\text{O}_3$  nanoparticles loadings on the morphology and microstructure of an interfacial layer structure formed between Al-bearing alloy and mild steel bimetal composite. Table 3 outlines experimental details for the development of  $\text{Al}_2\text{O}_3$  nanoparticles loaded in nano bimetallic composites. Figure 7 shows OM images of the cross-sections of mild steel substrate coated with Al-bearing alloy and Sn only (S1), and with 0.25% (S2), 0.50% (S3), 1% (S4), and 1.50% (S5)  $\text{Al}_2\text{O}_3$  nanoparticle-loaded Sn interlayers. It is worth noting that the interfacial layer microstructure and morphology were significantly influenced by adding the  $\text{Al}_2\text{O}_3$  nanoparticles in the Sn interlayer between Al-bearing alloy coating and mild steel substrate. An increase in the interfacial layer thickness by adding  $\text{Al}_2\text{O}_3$  nanoparticles was observed, as shown in Figure 7b–d. Moreover, the interfacial alloy layer formed is also regular and uniform over the entire Al-bearing and mild steel substrate interface. However, further increase in  $\text{Al}_2\text{O}_3$  nanoparticles to 1.50% resulted in the uneven and irregular morphology of the interfacial layer, as shown in Figure 7e.

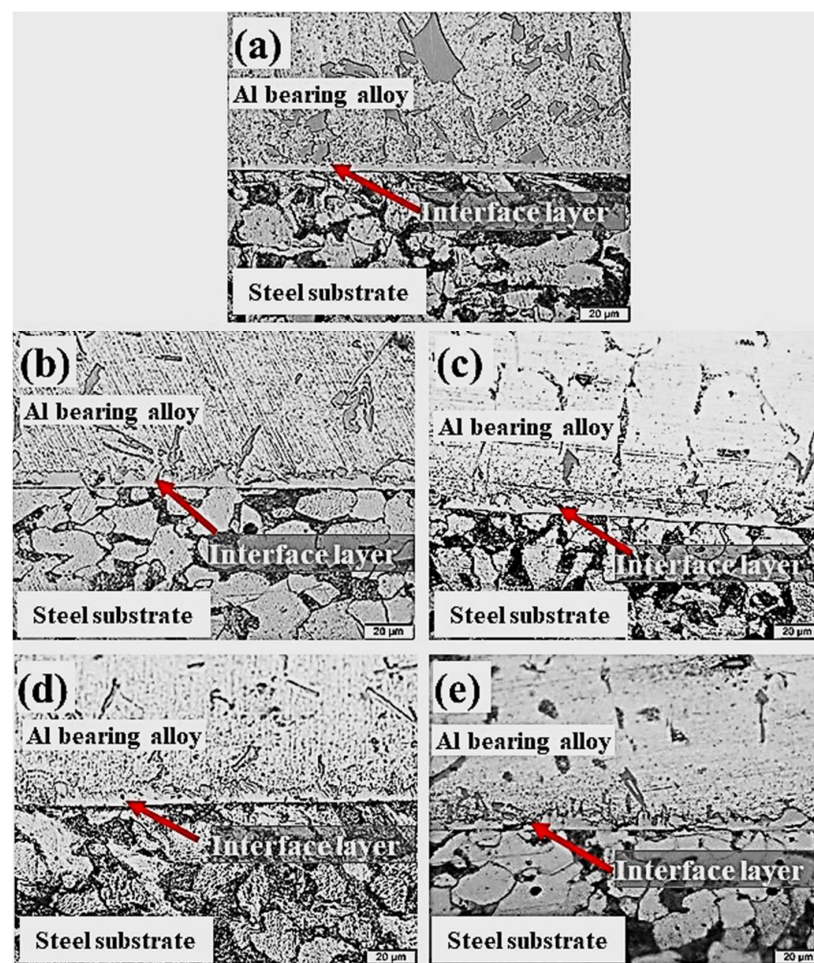


**Figure 7.** Cross-section microstructures of aluminum/steel bimetal with substrate pre-tinning using different interlayer composition: pure tin (S1) (a), tin with 0.25 wt.% (b), 0.50 wt.% (c) 1.00 wt.% (d), and 1.50 wt.% (e) (S2–S5) alumina nanoparticles, respectively.

Change in the thickness of the interfacial intermetallic compound (IMC) layer with  $\text{Al}_2\text{O}_3$  nanoparticles is shown in Figure 8. It is evident that the interfacial layer thickness increased with increasing the  $\text{Al}_2\text{O}_3$  nanoparticles from 0% to 1%. A further increase in  $\text{Al}_2\text{O}_3$  nanoparticles resulted in a decline in the interfacial layer thickness, as shown in Figure 8. Tikale and Prabhu [33] investigated the influence of  $\text{Al}_2\text{O}_3$  nanoparticles on the wetting and mechanical properties of low Ag lead-free SAC0307 solder alloy. An increase in wetting area, microhardness, and shear strength with low addition (from 0.01% to 0.50%) of  $\text{Al}_2\text{O}_3$  nanoparticles was reported. The findings of this study are in agreement with those reported in the literature [33].

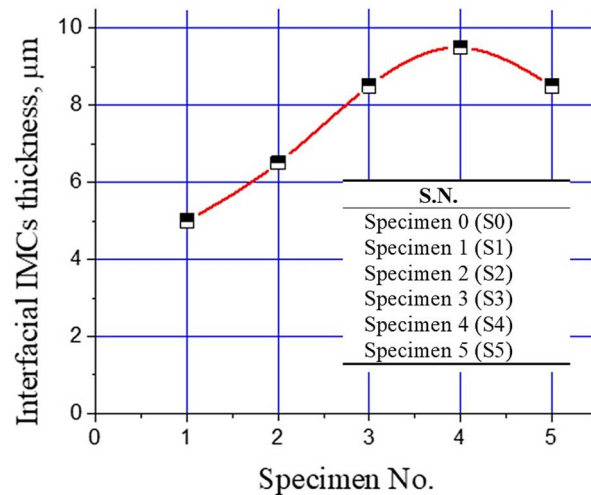


**Figure 8.** Plot of interfacial IMCs layer thickness for different bimetal castings prepared in this study.

It is suggested that the low addition of  $\text{Al}_2\text{O}_3$  nanoparticles increased wetting of the Sn and mild steel substrate, which facilitates a better interlayer bond. Subsequently, during the casting of molten Al-bearing alloy over  $\text{Al}_2\text{O}_3$  nanoparticles, the doped Sn layer facilitated the Al mass transfer to the steel substrate, where the following chemical reactions are inevitable [34–38]:



During the tinning process, Fe–Sn interfacial layer is developed. According to the Fe–Sn binary phase diagram,  $\text{FeSn}_2$ ,  $\text{FeSn}$ ,  $\text{Fe}_3\text{Sn}_2$ ,  $\text{Fe}_6\text{Sn}_3$  are the possible phases [38]. However,  $\text{FeSn}_2$  is commonly observed in the interface of tinned steels products.  $\text{FeSn}_2$  intermetallic is stable up to 496 °C, which contains 80.95% Sn [36,38]. It was expected that the  $\text{FeSn}_2$  layer would dissolve during the pouring of liquid Al bearing alloy at 770 °C. Reaction (1) was expected during the tinning process in this study. During the pouring of the molten Al-bearing alloy over the tinned steel substrate, reactions (2) were inevitable, developing the interfacial layer. However, by increasing  $\text{Al}_2\text{O}_3$  nanoparticles loadings, reaction (3) was also observed, which developed the second interfacial layer. The formation of  $\text{FeAlSi}$  IMCs according to Equation (4) was also possible, which has also been reported by earlier studies [31]. At low  $\text{Al}_2\text{O}_3$  nanoparticles loading, there is an increase in interfacial layer growth because nanoparticles are most likely embedded within the interfacial layer structure. However, at higher  $\text{Al}_2\text{O}_3$  nanoparticles loading, agglomeration obstructs the interfacial layer growth. As a result, the interfacial layer is irregular and less thickened. An optimum  $\text{Al}_2\text{O}_3$  nanoparticles loading of a maximum of 0.25% is one of the key findings of this study. Elemental mapping of the Al-bearing alloy and mild steel bimetal cross-section

in the case of pure Sn interlayer was obtained through the EDS analysis, which is presented in Figure 9. An SEM–SEI image of a cross-section showing Al-bearing alloy, interfacial layer, and mild steel substrate is given in Figure 9a. The corresponding elemental maps of Al, Si, Fe, and Sn are shown in Figure 9b–e.

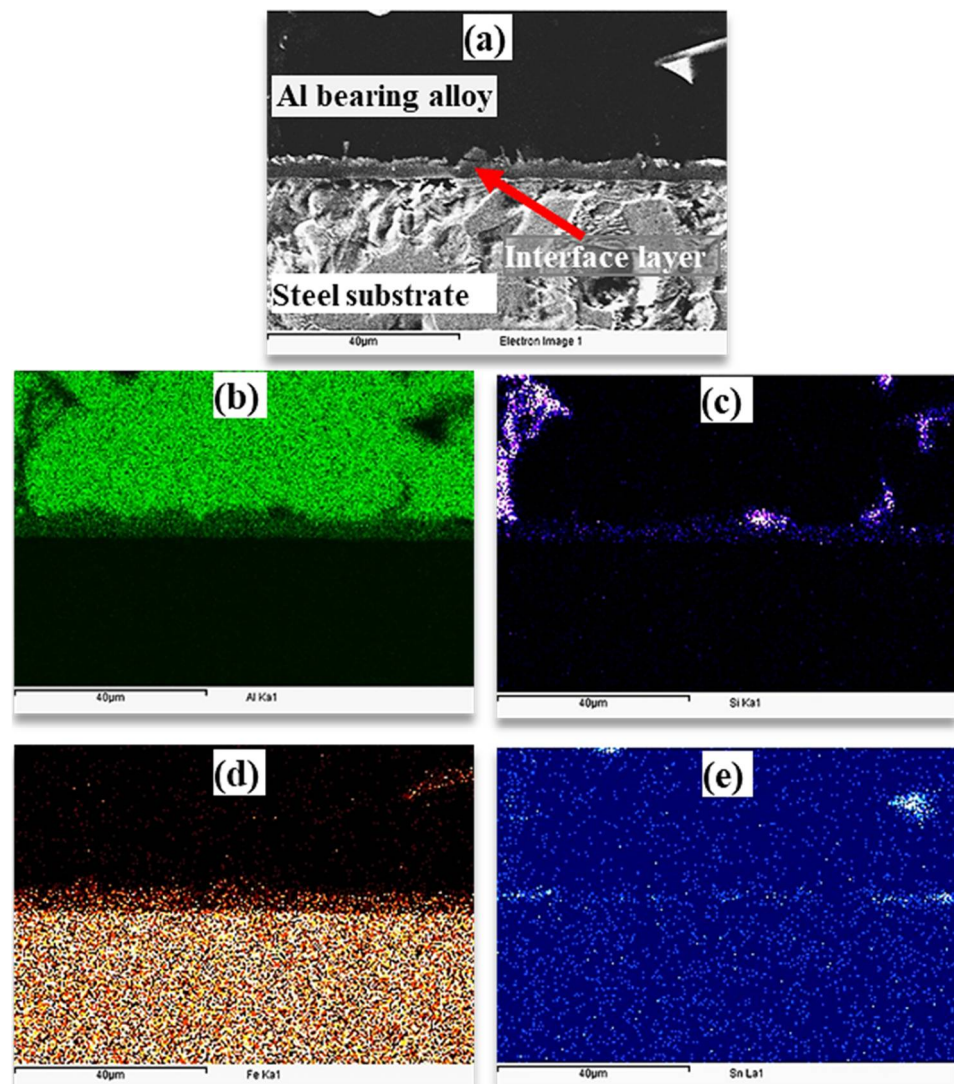


**Figure 9.** (a) SEM images of interfacial aluminum/steel bimetal using pure tin interlayer (S1) and (b–e) mapping analysis of Al, Si, Fe, and Sn elements, respectively.

It is clear that Al-bearing alloy is composed of Al, Si, and Sn, and steel substrate is composed of Fe, as expected. Additionally, it is evident from Figure 9 that the interfacial layer contains Al, Fe, and Si, with Sn segregation within the interlayer region. There is evidence of FeAlSi and Sn intermetallic particles but is difficult to distinguish at this stage.

EDS analysis was used to obtain interfacial layer point analysis, shown in Figures 10–12. Interfacial layer point analysis, shown in Figure 10b,c, corresponds to points 1 and 2, shown in Figure 10a. Al, Si, Fe, and Sn are the main components of the interfacial alloy layer. It is worth noting that the chemical composition of the interfacial alloy layer is uniform entirely. Therefore, it is suggested that the entire interfacial layer is composed of only one type of  $\text{Al}_5\text{Fe}_2/\alpha\text{-AlFeSi}$  IMCs particles. Such Fe-based IMCs particles have been reported in the Al–Zn–Si coating alloy [34].

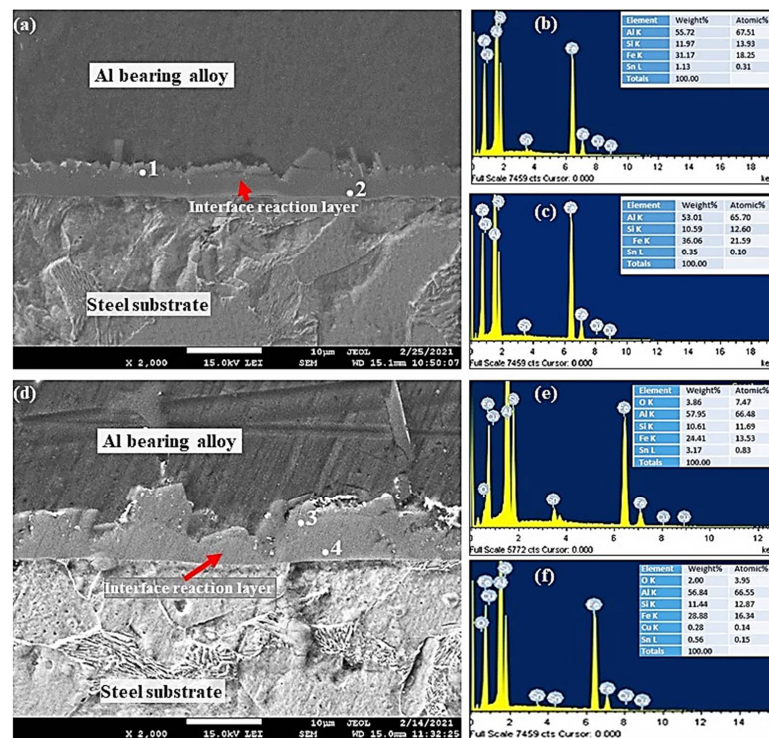


Figure 10. SEM micrographs and EDS from Al-bearing alloy/steel bimetallic composites: (a) SEM for bimetal with Sn interlayer (specimen 0); (b,c) EDS analysis of points 1 and 2 in (a), respectively; (d) SEM for bimetal with Sn + 0.25% Al<sub>2</sub>O<sub>3</sub> nanoparticles interlayer (specimen 1); (e,f) EDS analysis of points 3 and 4 in (d), respectively.

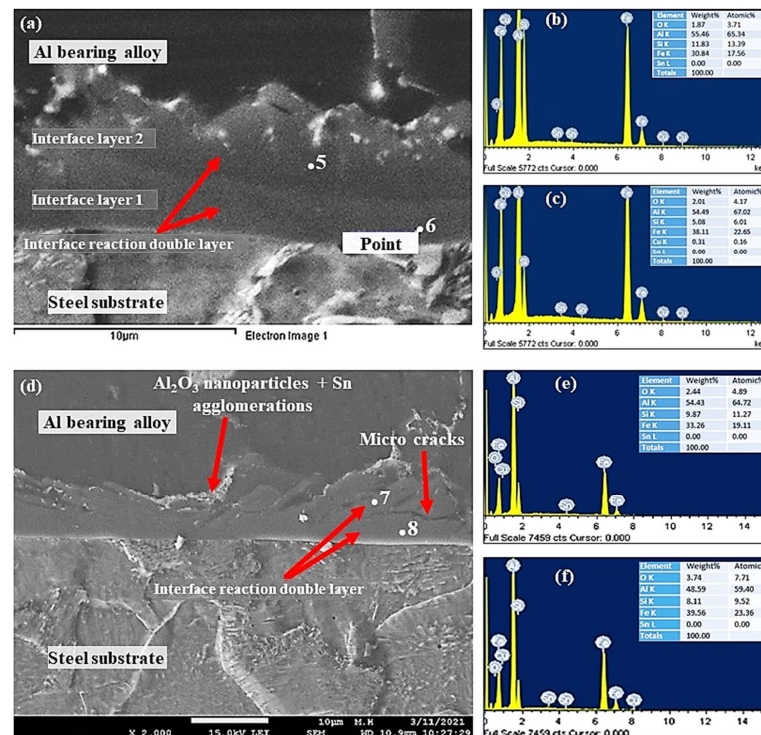
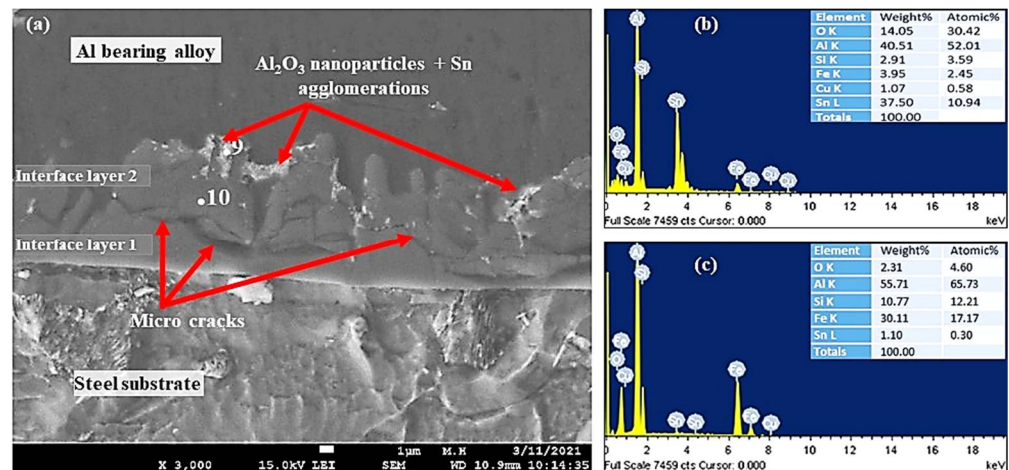


Figure 11. SEM micrographs and EDS from Al-bearing alloy/steel bimetallic composites: (a) SEM for bimetal with Sn + 0.50% Al<sub>2</sub>O<sub>3</sub> nanoparticles interlayer (specimen 3); (b,c) EDS analysis of points 5 and 6 in (a), respectively; (d) SEM for bimetal with Sn + 1.00% Al<sub>2</sub>O<sub>3</sub> nanoparticles interlayer (specimen 4); (e,f) EDS analysis of points 7 and 8 in (d), respectively.



**Figure 12.** SEM micrographs and EDS from Al-bearing alloy/steel bimetallic composites: (a) SEM for bimetal with Sn + 1.50%  $\text{Al}_2\text{O}_3$  nanoparticles interlayer (specimen 5); (b,c) EDS analysis of points 9 and 10 in (a), respectively.

Generally,  $\text{FeAl}_3$  and  $\text{Fe}_2\text{Al}_5$  are common IMCs phases observed in the Al and –Zn–Si coated steel products.  $\text{Fe}_5\text{Si}_2\text{Al}_{20}$  phase has been reported in the literature [31–33], which formed in the case of poorly coated steel samples. It is suggested, based on the point analysis, that the interfacial alloy is composed of  $\text{FeAl}_3$  or  $\alpha\text{-FeAlSi}$  phase (Table 4). EDS analysis of Points 3 and 4 of Figure 10d are shown in Figure 10e,f. Similar to S0, the interfacial alloy layer is composed of only one type of IMCs, which is most likely  $\text{Al}_{4.5}\text{SiFe}$ , in addition to  $\text{Al}_2\text{O}_3$  nanoparticles. The highly charged white spots in Figure 10d are  $\text{Al}_2\text{O}_3$  nanoparticles that are embedded within the interfacial layer.

**Table 4.** Results of EDS analysis for points indicated in Figures 6–8.

Point No.	Sample No.	Element Compositions (at. %)					Interface Layers Nos.	Interface Component
		Al	Fe	Si	Sn	O		
1		67.51	18.25	13.93	0.31	-		
2	1	65.70	21.59	12.60	0.10	-	1	$\text{Fe}_2\text{Al}_5$ , $\text{Al}_8\text{Fe}_2\text{Si}$
3		66.48	13.53	11.69	0.83	7.47		
4	2	66.55	16.34	12.87	0.15	3.93	1	$\text{Al}_{4.5}\text{SiFe}$ , $\text{Al}_2\text{O}_3$
5		65.34	17.56	13.39	-	3.71		
6	3	67.02	22.65	6.01	-	4.17	2	$\text{Fe}_2\text{Al}_5$ , $\text{Al}_8\text{Fe}_2\text{Si}$ , $\text{Al}_2\text{O}_3$
7		64.72	19.11	11.27	-	4.89		
8	4	59.40	23.36	9.52	-	7.71	2	$\text{FeAl}_3$ , $\text{Al}_2\text{Fe}_3\text{Si}_3$ , $\text{Al}_2\text{O}_3$
9		52.01	02.45	3.59	10.9	30.42		
10	5	65.73	17.17	12.21	0.30	4.60	2	$\text{Fe}_2\text{Al}_5$ , $\text{Al}_8\text{Fe}_2\text{Si}$ , $\text{Al}_2\text{O}_3$

The interfacial layer of samples S3 and S4 SEM–SEI images and EDS point analysis is shown in Figure 11. Surprisingly, two interfacial layers were observed by increasing  $\text{Al}_2\text{O}_3$  nanoparticles from 0.25% to 0.50% and above. Interfacial layer 1 was formed between the steel substrate and interface layer 2, which was formed between Al-bearing alloy and interface layer 1, as shown in Figure 11a. The interfacial alloy layer 1 is most likely  $\text{FeAl}_3$  based on the EDS and Fe–Al binary phase diagram. It should be noted that Si plays a significant role in altering the crystallography of  $\text{Al}_3\text{Fe}$ , and hence,  $\alpha\text{-Al}_8\text{Fe}_2\text{Si}$  IMC is possible in layer 1. The interfacial alloy 2 is  $\text{Al}_5\text{Fe}_2$  and  $\text{Al}_8\text{Fe}_2\text{Si}$ , as given in Table 4. Previous researchers have reported the formation of  $\text{Al}_3\text{Fe}$  adjacent to the steel surface and  $\text{Al}_5\text{Fe}_2$  adjacent to the Al–Zn–Si coating alloy [39].  $\text{FeAlSi}$  ( $\alpha\text{-Al}_8\text{Fe}_2\text{Si}$ / $\alpha\text{-Al}_{167.8}\text{Fe}_{44.9}\text{Si}_{23.9}$  IMC precipitation is also inevitable in the Al-bearing alloy containing Si [26]. In addition

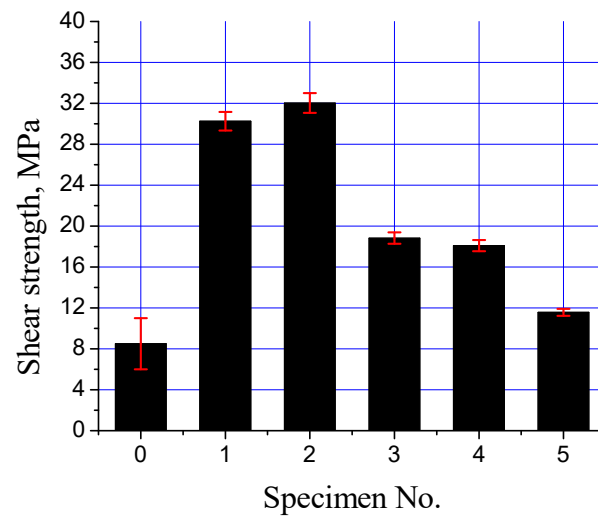
to the formation of two interfacial layers,  $\text{Al}_2\text{O}_3$  nanoparticles are also present within the layers, added initially in the Sn interlayer.

Figure 12 shows SEM–SEI and EDS analysis of the mild steel/Al-bearing alloy composite containing 1.50%  $\text{Al}_2\text{O}_3$  nanoparticles in the Sn interlayer. Similar to samples S3 and S4, two interfacial alloy layers were observed in this sample (S5).  $\text{AlFe}_3$  and  $\alpha\text{-AlFeSi}$  IMCs are dominated in interface layer 2, and  $\text{Al}_5\text{Fe}_2$  and  $\alpha\text{-AlFeSi}$  are found in interface layer 1, which is adjacent to the Al-bearing alloy. Additionally,  $\text{Al}_2\text{O}_3$  nanoparticles agglomerates and Sn precipitates (point 9) were also observed, as shown in Figure 12. Microcracks formation at the interfacial boundary layers 1 and 2 interface is yet another microstructural feature observed in this study, as shown in Figures 11d and 12a. A similar microcracks formation has been reported in the literature [40] during the study of 316 L stainless steel immersion in the Al–Zn–Si coating alloy. The interfacial layers formed are hard and brittle phases and hence tend to fracture at their interfaces [40]. This is one of the key parameters that contribute to the bottom cross build-up in a galvanizing bath.

### 3.3.2. Interfacial Mechanical Properties

The interfacial strength of the mild steel/Al-bearing alloy composites with various types of Sn +  $\text{Al}_2\text{O}_3$  nanoparticles interlayers was analyzed with a shear test. Figure 13 shows all samples (S0 to S5) shear strength plots. A drastic increase in the shear strength by improving the processing parameters is evident, improving the shear strength from ~8 to ~30 MPa (S0 and S1). The regular and uniform interfacial layer development is responsible for the improved shear strength. Moreover, shear strength increased by adding  $\text{Al}_2\text{O}_3$  nanoparticles in the Sn interlayer, as observed for S3. A low  $\text{Al}_2\text{O}_3$  nanoparticles addition in the Sn interlayer improved wetting between the mild steel substrate and Al-bearing alloy. Eventually, the shear strength of the bimetal composite containing Sn + 0.25%  $\text{Al}_2\text{O}_3$  nanoparticles increased by ~6%. Further increase in the  $\text{Al}_2\text{O}_3$  nanoparticles loading did not result in the same effect and even decreased the shear strength, as shown in Figure 13. By increasing  $\text{Al}_2\text{O}_3$  nanoparticles loading to 0.50%, shear strength declined by 43%. Two factors are responsible for the decline in the shear strength of high  $\text{Al}_2\text{O}_3$  nanoparticles bimetal composites: (1) uneven  $\text{Al}_2\text{O}_3$  nanoparticles distribution and agglomeration in the interfacial layer and (2) development of two types of interfacial layers. Both of these factors significantly reduced the shear strength of the high  $\text{Al}_2\text{O}_3$  nanoparticle-loaded bimetallic composites. During mechanical loading,  $\text{Al}_2\text{O}_3$  nanoparticles agglomerates act as weak regions, where localized stress exceeds the fracture strength of the interfacial IMC layer. In addition to that, two IMC interfacial layers formation is not recommended for better integrity of the mild steel/Al-bearing alloy bimetallic composite. As reported earlier, interfacial layers are much harder and brittle, compared with the substrate and coating alloy, hence observing different mechanical behavior under applied load. The modulus of elasticity for mild steel substrate, interfacial layers (1,2), and Al-bearing alloy are different. Moreover, microcracks development between interfacial layers 1 and 2 are also a weak point that can facilitate earlier failure, hence lowering the shear strength.

Table 5 summarizes the shear strength of the steel and Al bimetal composite having various interlayer materials and casting processes. The Sn and Sn + 0.25%  $\text{Al}_2\text{O}_3$  nanoparticles interlayer mild steel/Al-bearing alloy bimetal composite showed comparable shear strength with the Zn + 0.2% Bi interlayer Fe/Al bimetallic composites. Much higher shear strength of mild steel/Al-bearing alloy was obtained in this study, compared with most of the similar bimetal composites, as outlined in Table 5.



**Figure 13.** Interfacial shear strength of mild steel/Al-bearing alloy composites (S0 to S5).

**Table 5.** Reports on the shear property of Al/Fe bimetallic composites for different interlayer materials and deposition processes in the literature.

Interlayer Material	Shear Stress, MPa		
	Deposition Process		
	Hot Dipping	Electroplating	Direct Tinning
Brass	-	17.5 [41]	-
Al – 7.2 wt.% Si	08.5 [42]	-	-
Pure Zn	16.0 [42]	20.0 [23]	-
Zn + 0.2 wt.% Bi	32.0 [42]	-	-
Pure Sn	-	-	06.75 [28]
Pure Sn (process parameter B)	-	-	30.25 [this study]
Sn + 0.25% Al <sub>2</sub> O <sub>3</sub> Nanoparticles	-	-	32.03 [this study]

#### 4. Conclusions

In the present study, a steel/Al-bearing alloy bimetallic composite was developed with different loadings of Al<sub>2</sub>O<sub>3</sub> nanoparticles. The tinning process was optimized prior to the loading of Al<sub>2</sub>O<sub>3</sub> nanoparticles for better interfacial alloy development. The following features were the key findings of this study:

- The interfacial layer developed during tinning was composed of FeSn<sub>2</sub> that was stable up to a temperature of 496 °C [37]. In the case of low mold preheating (170 °C) and molten Al-bearing alloy (720 °C), the interfacial layer was irregular and not fully coherent and continuous. However, by increasing the mold's preheating temperature to 350 °C and Al-bearing alloy melting temperature to 770 °C, a regular, coherent, and continuous interfacial layer was successfully developed.
- An increase in Al-bearing alloy pouring temperature and mold preheat potentially dissolved the FeSn<sub>2</sub> layer. Consequently, mass transfer of the Al to the steel substrate increased, leading to the formation of a regular and continuous interfacial layer. The interfacial layer formed between the steel/Al-bearing composite was composed of Al<sub>5</sub>Fe<sub>2</sub>, in agreement with previous studies.
- By improving the process parameters, the shear strength of the steel/Al-bearing alloy surprisingly increased by 500%. The increase in the shear strain was 280%, which is also an extraordinary finding of this study.
- Further increase in the shear strength was recorded by loading 0.25% Al<sub>2</sub>O<sub>3</sub> nanoparticles in the Sn layer, and the findings are in agreement with the previous studies.

- Higher Al<sub>2</sub>O<sub>3</sub> nanoparticles loadings (0.50% to 1.50%) are not recommended due to Al<sub>2</sub>O<sub>3</sub> nanoparticles agglomerations between the interfacial layer and Al-bearing coating. Such microstructural discrepancies are sources of failure in materials, as they act as stress raiser points during loading.
- Two types of interfacial layers composed of AlFe<sub>3</sub> and Al<sub>5</sub>Fe<sub>2</sub> were observed by increasing Al<sub>2</sub>O<sub>3</sub> nanoparticles loadings to 0.50% and beyond. Heat accumulation and coating time are two key factors that facilitate the development of two layers instead of one. Moreover, AlFe<sub>3</sub> formed adjacent to the steel substrate, and Al<sub>5</sub>Fe<sub>2</sub> formed close to the Al-bearing alloy.

**Author Contributions:** Conceptualization, M.R., K.S.A.H. and A.K.; methodology, M.R. and K.M.H. validation, M.R., A.S.A., N.F. and A.K.; formal analysis, M.R., A.K. and N.F.; investigation, F.A.H., B.A. and K.M.H.; resources, N.F., M.R. and B.A.; data curation, M.R. and A.K.; writing—original draft preparation, M.R. and A.K.; writing—review and editing, A.S.A., K.M.H., K.S.A.H. and F.A.H.; project administration, A.S.A. All authors have read and agreed to the published version of the manuscript.

**Funding:** This research has been funded by the Scientific Research Deanship at the University of Ha'il—Saudi Arabia through project number RG-20074.

**Data Availability Statement:** Data available in a publicly accessible.

**Conflicts of Interest:** The authors declare no conflict of interest.

## References

1. Ramadan, M.; El-Bagoury, N.; Fathy, N.; Waly, M.A.; Nofal, A.A. Microstructure, fluidity, and mechanical properties of semi-solid processed ductile iron. *J. Mater. Sci.* **2011**, *46*, 4013–4019. [[CrossRef](#)]
2. Ramadan, M.; Nofal, A.A.; Elmahalawi, I.; Abdel-Karim, R. Influence of graphite nodularity on microstructure and processing window of 1.5% Ni-0.3% Mo austempered cast iron. *Mater. Sci. Eng. A* **2006**, *435*, 564–572. [[CrossRef](#)]
3. Ramadan, M.; Fathy, N. Solidification microstructure of rheocast hyper-eutectic Al–18Si alloy. *J. Metall. Eng.* **2013**, *2*, 149–153.
4. Gawronski, J.; Szajnar, J.; Wrobel, P. Study on theoretical bases of receiving composite alloy layers on surface of cast steel castings. *J. Mater. Process. Technol.* **2004**, *157*, 679–682. [[CrossRef](#)]
5. Tayal, R.K.; Kumar, S.; Singh, V.; Garg, R. Characterization and microhardness evaluation of A356/Mg joint produced by vacuum-assisted sand mold compound casting process. *Int. J. Metalcast.* **2019**, *13*, 392–406. [[CrossRef](#)]
6. Tayal, R.K.; Kumar, S.; Singh, V.; Gupta, A.; Ujjawal, D. Experimental investigation and evaluation of joint strength of A356/ Mg bimetallic fabricated using compound casting process. *Int. J. Metalcast.* **2019**, *13*, 686–699. [[CrossRef](#)]
7. Kmita, A.; Dańko, R.; Holtzer, M.; Hutera, B.; Stypuła, B. Utilisation of nanoparticles in technologies of producing castings for the needs of power engineering. *Nanomater. Energy* **2014**, *3*, 53–60. [[CrossRef](#)]
8. Bawane, K.; Lu, K. Microstructure evolution of nanostructured ferritic alloy with and without Cr<sub>3</sub>C<sub>2</sub> coated SiC at high temperatures. *J. Mater. Sci. Technol.* **2020**, *43*, 126–134. [[CrossRef](#)]
9. Jiang, S.H.; Wang, H.; Wu, Y.; Liu, X.; Chen, H.; Yao, M.; Gault, B.; Ponge, D.; Raabe, D.; Hirata, A.; et al. Ultrastrong steel via minimal lattice misfit and high-density nanoprecipitation. *Nature* **2017**, *544*, 460–464. [[CrossRef](#)] [[PubMed](#)]
10. Rodríguez, E.; Pérez, A.; Mercado-Solis, R.D.; Abraham, V.-T.; Jiménez, O.; Flores, M.; González, M.A.; Ibarra, J. Erosion problem in tool steel using cold box core-making process. *China Foundry* **2019**, *16*, 204–210. [[CrossRef](#)]
11. Han, X.; Zhang, Z.P.; Hou, J.Y.; Barber, G.C.; Qiu, F. Tribological behavior of shot peened/austempered AISI 5160 steel. *Tribol. Int.* **2020**, *106197*, 145. [[CrossRef](#)]
12. Li, H.C.; Liu, Y.X.; Zhang, Y.H.; Liu, Z.; Zhai, Q.-J. Effects of hot top pulsed magneto-oscillation on solidification structure of steel ingot. *China Foundry* **2018**, *15*, 110–116. [[CrossRef](#)]
13. Hao, L.H.; Ji, X.; Zhang, G.Q.; Zhao, W.; Sun, M.; Peng, Y. Carbide precipitation behavior and Mechanical properties of micro-alloyed medium Mn steel. *J. Mater. Sci. Technol.* **2020**, *47*, 122–130. [[CrossRef](#)]
14. Liu, Y.C.; Liu, C.X.; Sommer, F.; Mittemeijer, E.J. Martensite formation kinetics of substitutional Fe–0.7at.% Al alloy under uniaxial compressive stress. *Acta Mater.* **2015**, *98*, 164–174. [[CrossRef](#)]
15. Zhang, H.J.; Li, C.; Guo, Q.Y.; Ma, Z.; Li, H.; Liu, Y. Improving creep resistance of nickel-based superalloy Inconel 718 by tailoring gamma double prime variants. *Scr. Mater.* **2019**, *164*, 66–70. [[CrossRef](#)]
16. Zhang, K. Design of real time monitor system of manufacture process of iron and steel industry based on new style sensors. *Energy Procedia Part A* **2012**, *16*, 627–632. [[CrossRef](#)]
17. Melchers, R.E. Long-term corrosion of cast irons and steel in marine and atmospheric environments. *Corros. Sci.* **2013**, *68*, 186–194. [[CrossRef](#)]

18. Chen, B.; Yang, J.X.; Ouyang, Z.Y. Life cycle assessment of internal recycling options of steel slag in Chinese iron and steel industry. *J. Iron Steel Res. Int.* **2011**, *18*, 33–40. [[CrossRef](#)]
19. Qiu, F.; Liu, T.-S.; Zhang, X.; Chang, F.; Shu, S.-L.; Yang, H.-Y.; Zhao, Q.-L.; Jiang, Q.-C. Application of nanoparticles in cast steel: An overview. *China Foundry* **2020**, *17*, 111–126. [[CrossRef](#)]
20. Ramadan, M. Interface characterization of bimetallic casting with a 304 stainless steel surface layer and a gray cast iron base. *Adv. Mater. Res.* **2015**, *1120*, 993–998. [[CrossRef](#)]
21. Wróbel, T. Bimetallic layered castings alloy steel–gray cast iron. *Arch. Mater. Sci. Eng.* **2011**, *48*, 118–125.
22. Zhao, J.; Zhao, W.; Qu, S.; Zhang, Y. Microstructures and mechanical properties of AZ91D/0Cr19Ni9 bimetal composite prepared by liquid–solid compound casting. *Trans. Nonferrous Met. Soc. China* **2019**, *29*, 51–58. [[CrossRef](#)]
23. Shin, J.; Kim, T.; Lim, K.; Cho, H.; Yang, D.; Jeong, C.; Yi, S. Effects of steel type and sandblasting pretreatment on the solid-liquid compound casting characteristics of zinc-coated steel/aluminum bimetal. *J. Alloys Compd.* **2019**, *778*, 170–185. [[CrossRef](#)]
24. Fathy, N.; Ramadan, M. Influence of volume ratio of liquid to solid and low pouring temperature on interface structure of cast Babbitt-steel bimetal composite. *AIP Conf. Proc.* **2018**, *1966*, 020028. [[CrossRef](#)]
25. Ramadan, M.; Alghamdi, A.S.; Subhani, T.; Halim, K.S.A. Fabrication and characterization of Sn-based babbitt alloy nanocomposite reinforced with Al<sub>2</sub>O<sub>3</sub> nanoparticles/carbon steel bimetallic material. *Materials* **2020**, *13*, 2759. [[CrossRef](#)]
26. Ramadan, M.; Ayadi, B.; Rajhi, W.; Alghamdi, A.S. Influence of Tinning Material on Interfacial Microstructures and Mechanical Properties of Al12Sn4Si1Cu /Carbon Steel Bimetallic Castings for Bearing Applications. *Key Eng. Mater.* **2020**, *835*, 108–114. [[CrossRef](#)]
27. Ramadan, M.; Hafez, K.M.; Alghamdi, A.S.; Ayadi, B.; Halim, K.S.A. Novel Approach for Using Ductile Iron as Substrate in Bimetallic Materials for Higher Interfacial Bonding Bearings. *Inter. Met. Cast* **2021**, *11*, 145.
28. Ramadan, M.; Alghamdi, A.S.; Hafez, K.M.; Subhani, T.; Halim, K.S.A. Development and Optimization of Tin/Flux Mixture for Direct Tinning and Interfacial Bonding in Aluminum/Steel Bimetallic Compound Casting. *Materials* **2020**, *13*, 5642. [[CrossRef](#)] [[PubMed](#)]
29. Alghamdi, A.S.; Halim, K.S.A.; Amin, M.A.; Alshammari, A.S.; Fathy, N.; Ramadan, M. Interfacial Microstructure and Corrosion Behaviour of Mild Steel Coated with Alumina Nanoparticles Doped Tin Composite via Direct Tinning Route. *Coatings* **2021**, *11*, 1318. [[CrossRef](#)]
30. Ayadi, B.; Ramadan, M. Novel and simple technique for interfacial shear strength of liquid-solid compound casting specimen. *Mater. Today Proc.* **2021**, *47*, 2299–2304. [[CrossRef](#)]
31. Khaliq, A.; Parker, D.J.; Setargew, N.; Qian, M. Fabrication of the  $\tau$ 5c Intermetallic Compound Monoliths by a Novel Powder Metallurgy and Hot Dipping Approach. *J. Metall. Mater. Trans. B* **2020**, *51*, 836–849. [[CrossRef](#)]
32. Khaliq, A.; Parker, D.J.; Setargew, N.; Kondoh, K.; Qian, M. Dissolution Kinetics of Iron-based Intermetallic Compounds ( $\tau$ 5c IMCs) in a Commercial Steel Strip Metallic Alloy Coating Process. *J. Metall. Mater. Trans. B* **2021**, *52*, 41–50. [[CrossRef](#)]
33. Tikale, S.; Prabhu, K.N. Development of low-silver content SAC0307 solder alloy with Al<sub>2</sub>O<sub>3</sub> nanoparticles. *Mater. Sci. Eng. A* **2020**, *787*, 139439. [[CrossRef](#)]
34. Durandet, Y.; Strezov, L.; Ebrill, N. Formation of Al–Zn–Si Coatings on Low Carbon Steel Substrates. *Galvatech* **1998**, *98*, 147–152.
35. Raghavan, V. Al-Fe-Si (Aluminum-Iron-Silicon). *J. Phase Equilibria* **2002**, *23*, 184–188. [[CrossRef](#)]
36. Tenaris, M.G.; Egli, W.A.; Perez, T.; Zubimendi, J.L.; Benítez, G.J. Formation of an Fe-Sn Intermetallic Layer During the Reflow Process After Tin Plating. *Plat. Surf. Finish.* **2003**, *90*, 44–49.
37. Dionisio, P.H.; de Barros, B.A.S., Jr.; Baumvol, I.J.R. Intermetallic phases formed during tin implantation into iron and steels. *J. Appl. Phys.* **1984**, *55*, 4219–4224. [[CrossRef](#)]
38. Kumar, K.C.H.; Wollants, P.; Delaey, L. Thermodynamic evaluation of Fe-Sn phase diagram. *Calphad* **1996**, *20*, 139–149. [[CrossRef](#)]
39. Setargew, N.; Hodges, J.; Parker, D. Dross Intermetallic Formation and the Alloy Layer in 55%Al-Zn Coating Systems. In Proceedings of the Steel Research Hub–Program C Meeting, Wollongong, Australia, 18 December 2015.
40. Khaliq, A.; Subhani, T.; Ali, H. Analysis of 316L Stainless Steel Interaction with Galvanizing Alloy Bath. *Microsc. Microanal.* **2020**, *26*, 2884–2886. [[CrossRef](#)]
41. Raja, V.; Kavitha, M.; Chokkalingam, B.; Ashraya, T.S. Effect of Interlayers on Mechanical Properties of Aluminium Casting over Stainless Steel Pipe for Heat Exchanger Applications. *Trans. Indian Inst. Met.* **2020**, *73*, 1555–1560. [[CrossRef](#)]
42. Guo, Z.; Liu, M.; Bian, X.; Liu, M.; Li, J. An Al–7Si alloy/cast iron bimetallic composite with super-high shear strength. *J. Mater. Res. Technol.* **2019**, *8*, 3126–3136. [[CrossRef](#)]